Electronic Supplementary Material (ESI) for Journal of Materials Chemistry A.

Phase Control of Ultrafine FeSe Nanocrystals in N-doped Carbon Matrix for Highly Efficient and Stable Oxygen Reduction Reaction

Yangfei Cao,[a] Senchuan Huang,[a] Zhangquan Peng,[b] Fen Yao,[a] Xiaohui Li,[a] Yan Liu,[c] Haitao Huang,[, c] Mingmei Wu*[, a]*

[a] MOE Key Laboratory of Bioinorganic and Synthetic Chemistry, School of Chemistry/School of Marine Sciences, Sun Yat-sen University, Guangzhou/Zhuhai, 510275/519082, P. R. China.

[b] State Key Laboratory of Electroanalytical Chemistry, Changchun Institute of Applied Chemistry, Chinese Academy of Sciences, Changchun 130022, P. R. China.

[c] Department of Applied Physics, The Hong Kong Polytechnic University, Hong Kong, P. R. China.

***Corresponding authors:** aphhuang@polyu.edu.hk (Prof. H. Huang)

ceswmm@mail.sysu.edu.cn (Prof. M. Wu)

Experimental Section

Chemicals and Reagents

Ferric trichloride hexahydrate ($FeCl_3 \cdot 6H_2O$), pyrrole, selenium (Se) powder, potassium hydroxide, methanol, isopropanol and absolute ethanol were all purchased from Aladdin. Commercial Pt/C (20 *wt.* % Pt) catalyst and Nafion solution were obtained from Johnson Matthey and Sigma-Aldrich, respectively. All the chemical and reagents were used as received without further treatment. Deionized water (over 18 MΩ cm in resistivity) was employed throughout the experiments.

Table S1. Detailed synthetic parameters/conditions for different materials in this work.

Materials	*T* [°C]	*n* ($FeCl_3$) [mmol][a)]	*n* (Pyrrole) [mmol][a)]	*R* ($FeCl_3$/Pyrrole)	*n* (Se) [mmol][a)]
FeSe@NC-700	700	22.08	9.20	2.4/1	22.08
FeSe@NC-800	800	22.08	9.20	2.4/1	22.08
FeSe@NC-900	900	22.08	9.20	2.4/1	22.08
FeSe@NC-1000 (FeSe@NC-R_2)	1000	22.08	9.20	2.4/1	22.08
FeSe@NC-R_1	900	9.20	9.20	1/1	9.20
FeSe@NC-R_3	900	27.06	9.20	3/1	27.06
FeSe@NC-R_4	900	36.08	9.20	4/1	36.08

[a)] *n* is the moles of the chemical. FeSe@NC-900 and FeSe@NC-R_2 represents the same material.

Calibration of Reference Electrode

To avoid the influence of potential shift of Ag/AgCl reference electrode (RE) on the testing potential correction, a calibration experiment of RE was carried out in H_2-saturated electrolyte (0.1 M KOH) prior to the electrochemical measurements by referring to the reported literature (*Nat. Mater.* 2011, 10, 780-786; *Adv. Funct. Mater.*

2017, 27, 1606585). Specifically, a CV test was carried out within the potential window of -0.90 to -1.0 V (*vs.* Ag/AgCl) at the scan rate of 5 mV s^{-1} (Fig. S1). Platinum foil (1 cm^2 dipped into the solution) and platinum wire (0.25 mm diameter) were served as the working and counter electrodes, respectively. The electrolyte was kept purging with high-purity H_2 before and during the CV test. In the CV curve, the potentials at zero current were regarded as the thermodynamic values for hydrogen electrode reactions (-0.961 and -0.965 V at the negative and positive scan segments, respectively). Then the average value (0.963 V) was taken as the real potential difference between saturated Ag/AgCl reference electrode and reversible hydrogen electrode (RHE). It was only 4 mV smaller than the theoretical value of 0.967 V (i.e., 0.197+0.0592×13). Thus, all the electrochemical measurements were regarded reliable by using this RE with the calibration value of 0.963 V.

Computational Method

The geometrical optimization and energy calculations were performed using CASTEP (Cambridge Sequential Total Energy Package) module in Material Studio. The Perdew-Burke-Ernzerhof (PBE) exchange-correlation functional within the generalized gradient approximation (GGA) was employed. The wave functions at each *k*-point were expanded with a plane wave basis set. The cutoff energy for geometrical optimization and energy calculations was set to be 340 eV. A default Monkhorst-Pack *k*-point grid was used to sample the Brillouin zone integration. For band structure and density of states (DOS) calculations, separate XC-functional were used. The

convergence criterion of the electronic structure interaction and maximum force on each atom were set to be 1.0×10^{-6} eV atom^{-1} and 0.05 eV Å^{-1}, respectively.

FeSe models for calculations possessed hexagonal (NiAs-type, *P*6$_3$/*mmc*) or tetragonal (PbO-type, *P*4/*nmm*) structures. Prior to the energy calculations of various models, all the models were optimized to get the lowest energy. The 2*2*1 FeSe (101) supercell was used as model for studying atoms/molecules adsorption. A vacuum slab of 15 Å along the *c* axis and normal to the sheer was employed to avoid periodic interactions. For the calculation of O_2-adsorption energy (Δ*E*) on FeSe (101), Equation S1 was used:

$$\Delta E = E(\text{FeSe-O}_2) - E(\text{FeSe}) - E(\text{O}_2) \qquad \text{S1}$$

where *E*(FeSe-O_2), *E*(FeSe) and *E*(O_2) are enthalpies of optimized models for FeSe-O_2, FeSe and O_2, respectively.

According to the experimental results, O_2 reduction on FeSe@NCs underwent a four-electron transfer process with low HO_2^- yield in 0.1 M KOH electrolyte. The mechanisms can be written as:

Step 1: $^* + \mathrm{O}_2 + H_2O(l) + e^- \rightarrow HOO^* + OH^-$

Step 2: $HOO^* + e^- \rightarrow O^* + OH^-$

Step 3: $O^* + H_2O(l) + e^- \rightarrow HO^* + OH^-$

Step 4: $HO^* + e^- \rightarrow {}^* + OH^-$

Total reaction: $O_2(g) + 2H_2O(l) + 4e^- \rightarrow 4OH^-$

The change in Gibbs free energy (Δ*G*) of every step can be calculated by Equation S2:

$$\Delta G = \Delta E + \Delta E_{ZPE} - T\Delta S + \Delta G_U + \Delta G_{pH} \qquad \text{S2}$$

where ΔE means change of reaction energy, ΔE_{ZPE} is change of zero-point energy, T is temperature (298 K), and ΔS is change of entropy. $\Delta G_U = eU$, where U is equilibrium potential for O_2 to OH^- (U = 0.461 V). ΔG_{pH} = 0.0592*pH, where pH is equal to 13. Some thermodynamic data, such as entropies and zero-point energies of molecules (O_2, H_2, H_2O, *etc.*) in the gas phase, were taken from the NIST database.

Supplementary Figures

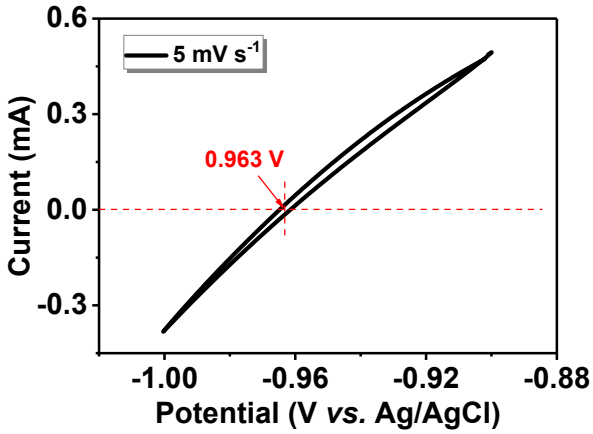

Fig. S1 CV curve of the calibration experiment for Ag/AgCl reference electrode in H_2-saturated 0.1 M KOH electrolyte.

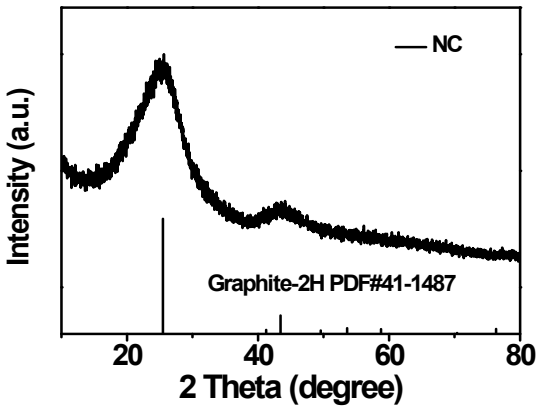

Fig. S2 XRD pattern of NC.

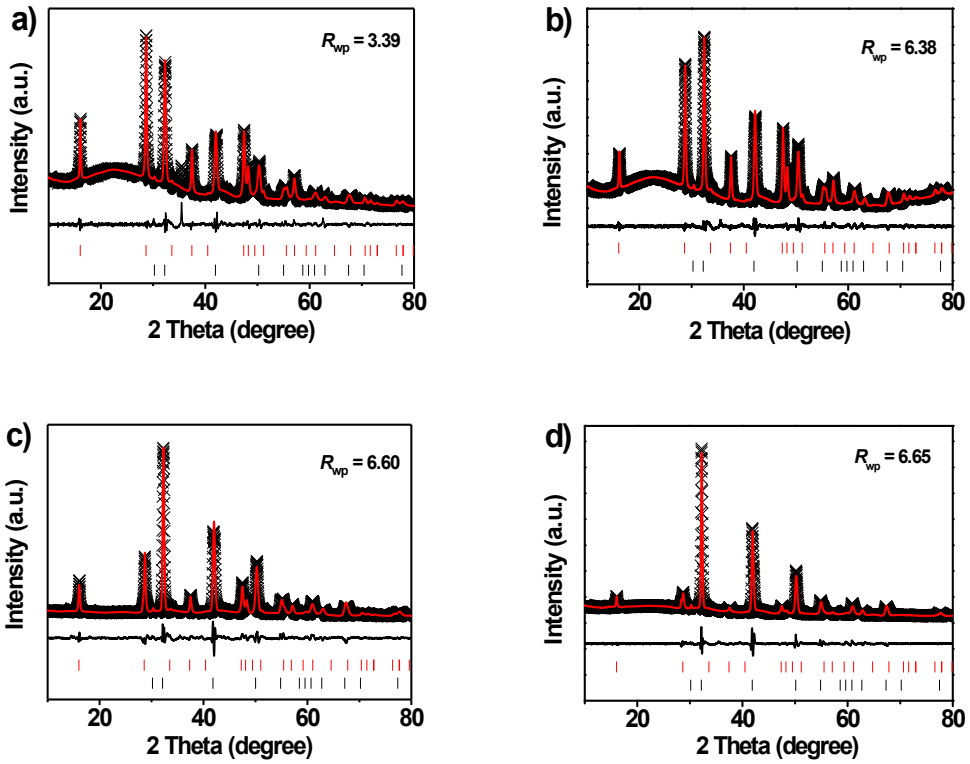

Fig. S3 Refined XRD patterns for FeSe@NC-*T* materials: a) FeSe@NC-700, b) FeSe@NC-800, c) FeSe@NC-900 and d) FeSe@NC-1000. The black and red standard lines represent *h*-FeSe and *t*-FeSe, respectively.

The relative percentages of *h*-FeSe : *t*-FeSe in Fig. S2a-d are 46.8 % : 53.2 %, 51.1 % : 48.9 %, 70.8 % : 28.2 %, 80.5 % : 19.5 %, respectively.

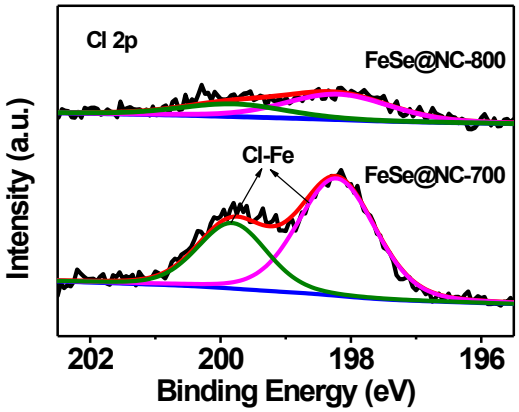

Fig. S4 Cl 2p XPS spectra of FeSe@NC-700 and FeSe@NC-800.

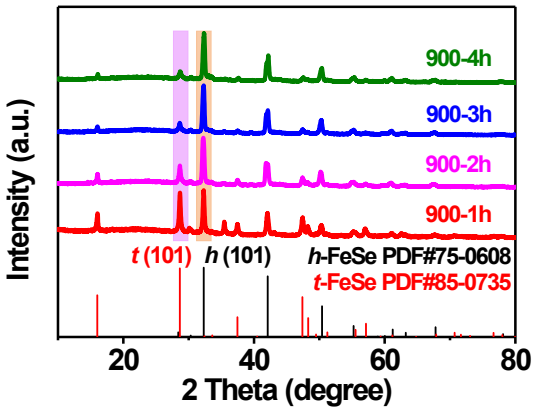

Fig. S5 XRD patterns of the materials prepared by annealing the Cl-Fe-PPy precursor of FeSe@NC-900 for different time (t_p = 1, 2, 3 and 4 h) at 900 °C.

The material denoted as "900-2h" is identical to FeSe@NC-900. With longer pyrolysis time, the relative intensity of *t*-(101) to *h*-(101) gradually decreases, indicating the tendency of phase transition from tetragonal to hexagonal FeSe. Thus, we concluded that *h*-FeSe was thermodynamically more stable than *t*-FeSe.

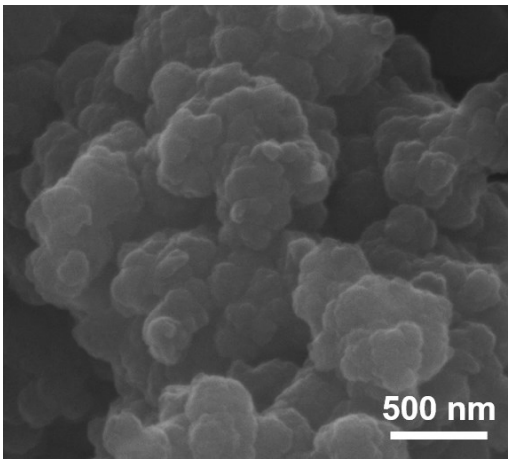

Fig. S6 SEM image of NC.

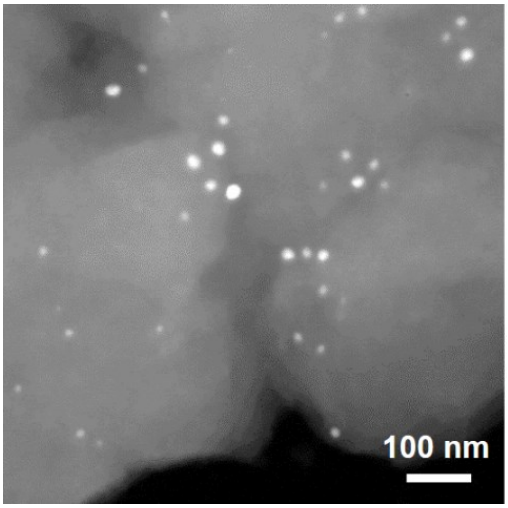

Fig. S7 High-angle annular dark field (HAADF) image of FeSe@NC-900. The bright dots are ultrafine FeSe nanocrystals.

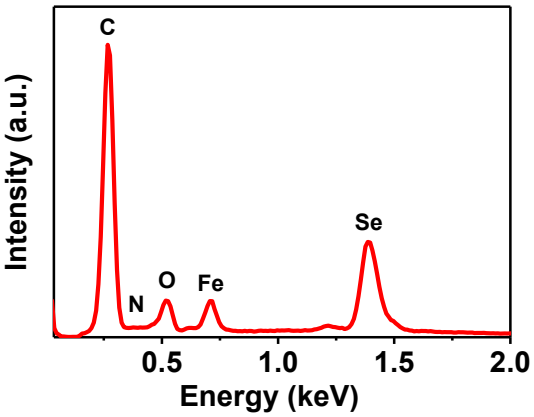

Fig. S8 EDX analysis of FeSe@NC-900.

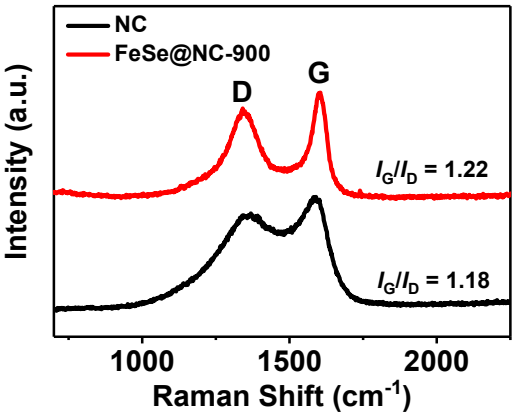

Fig. S9 Raman spectra of NC and FeSe@NC-900.

The characteristic peaks at 1342 and 1604 cm^{-1} represent the disorder structure/structural defects (D band) and in-plane stretching vibrations of graphitic carbon (G band), respectively.

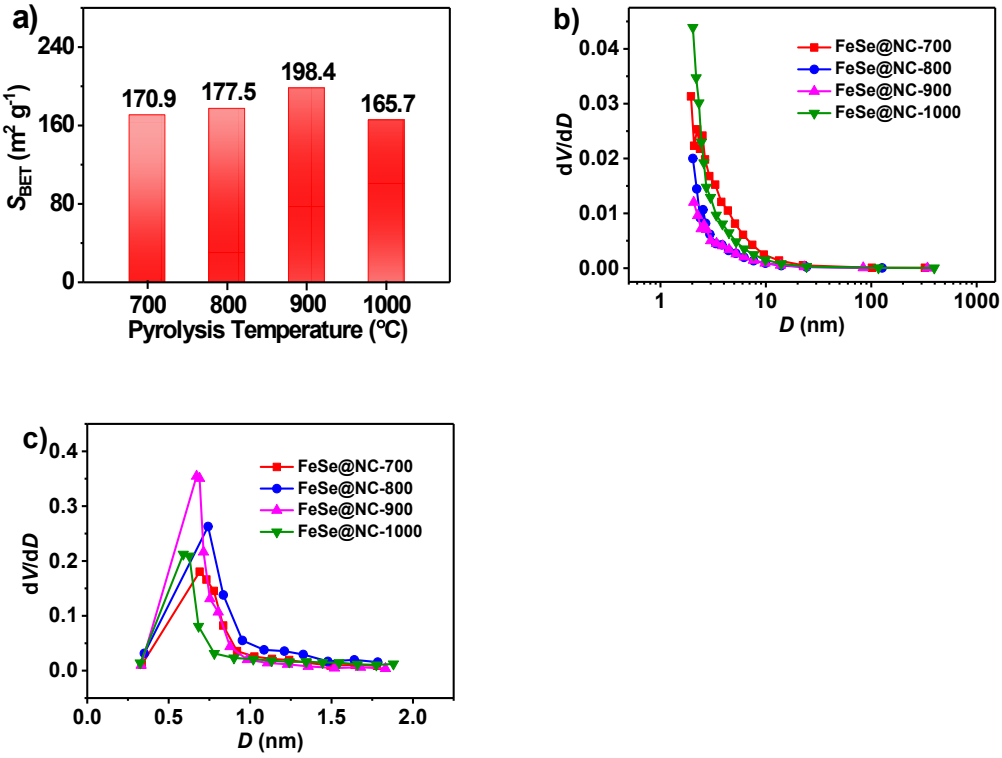

Fig. S10 a) BET surface areas and b,c) pore size distribution curves of mesopores/ macropores and micropores for FeSe@NC-*T* materials.

All FeSe@NC-*T* (*T* = 700, 800, 900 and 1000 °C) materials have large BET surface areas because of abundant micropores. Since these micropores are mainly resulted from the thermal decomposition of PPy, the BET surface areas of different FeSe@NC-*T* materials are very close. The pore size distribution curves of mesopores/macropores were calculated from the adsorption branches by BJH method, while those of micropores were analyzed by HK method. These pore size distribution curves confirmed the existence of abundant micropores.

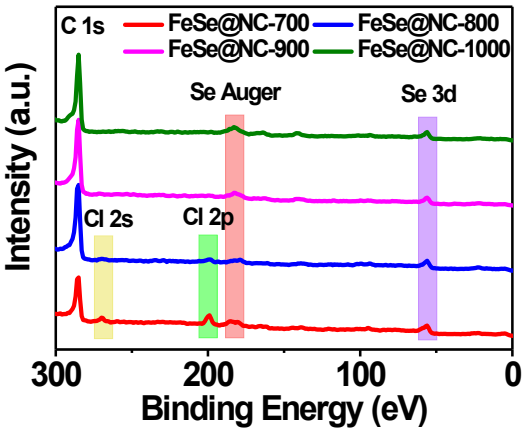

Fig. S11 Enlarged XPS survey spectra of FeSe@NC-*T* materials.

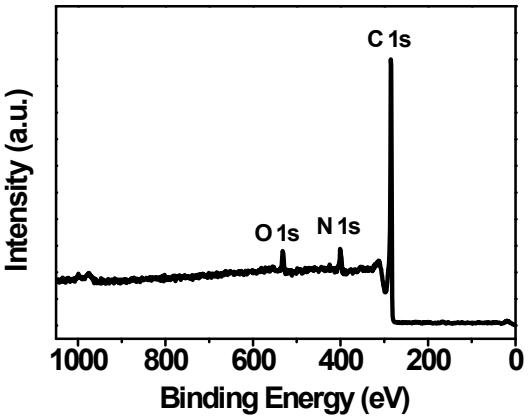

Fig. S12 XPS survey spectrum of NC. As expected, only C, N and O elements were detected.

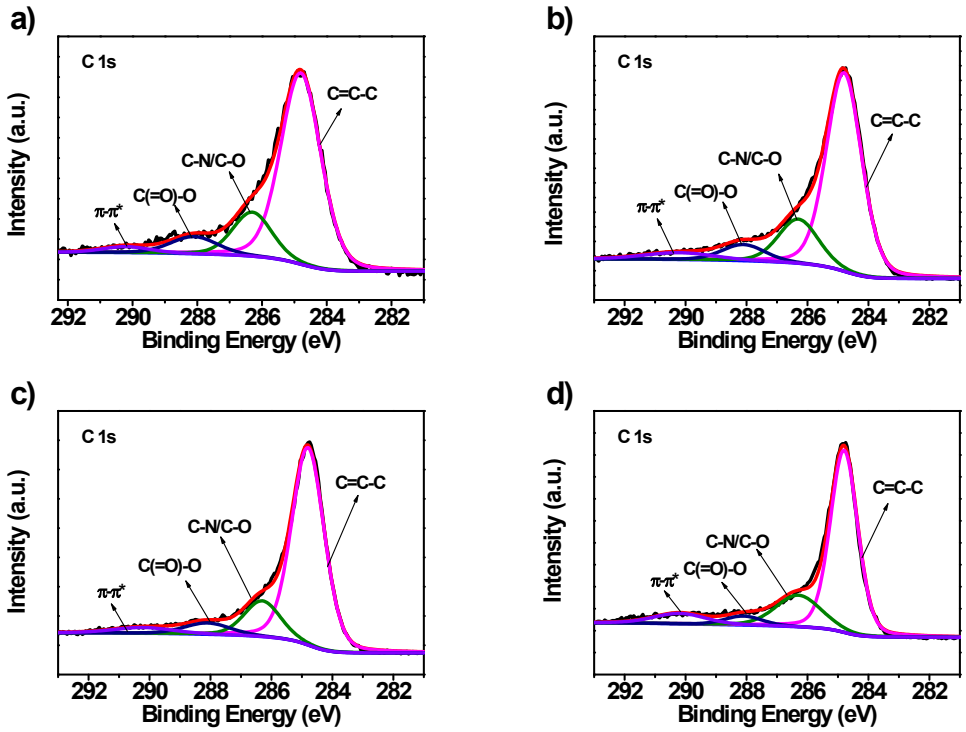

Fig. S13 High-resolution XPS spectra of C 1s for a) FeSe@NC-700, b) FeSe@NC-800, c) FeSe@NC-900 and d) FeSe@NC-1000.

All the C 1s spectra were deconvoluted into four peaks, assigning to C=C-C (284.8 eV), C-N (286.3 eV), C(=O)-O (288.1 eV) and π-π* (290.2 eV) species. The existence of C-N moiety suggested N-doped feature of carbon matrix.

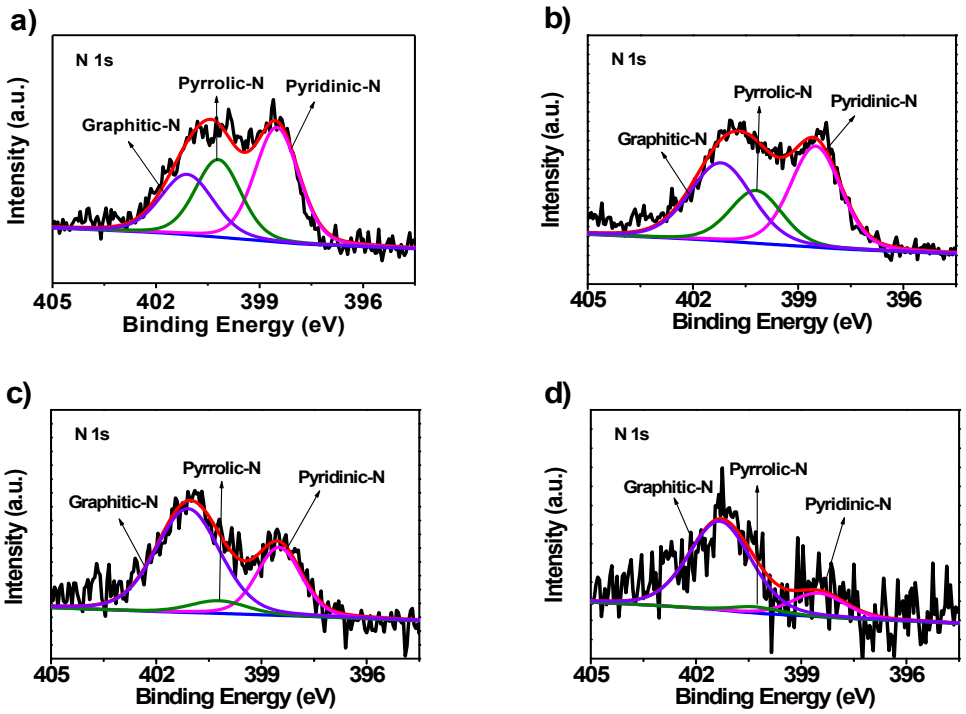

Fig. S14 High-resolution XPS spectra of N1s for a) FeSe@NC-700, b) FeSe@NC-800, c) FeSe@NC-900 and d) FeSe@NC-1000.

All the N 1s spectra were deconvoluted into three peaks, associated with pyridinic-N (398.5 eV), pyrrolic-N (400.2 eV) and graphitic-N (401.1 eV) moieties. With increasing pyrolysis temperature from 700 to 1000 °C, the percentage of pyrrolic-N moiety gradually decreased.

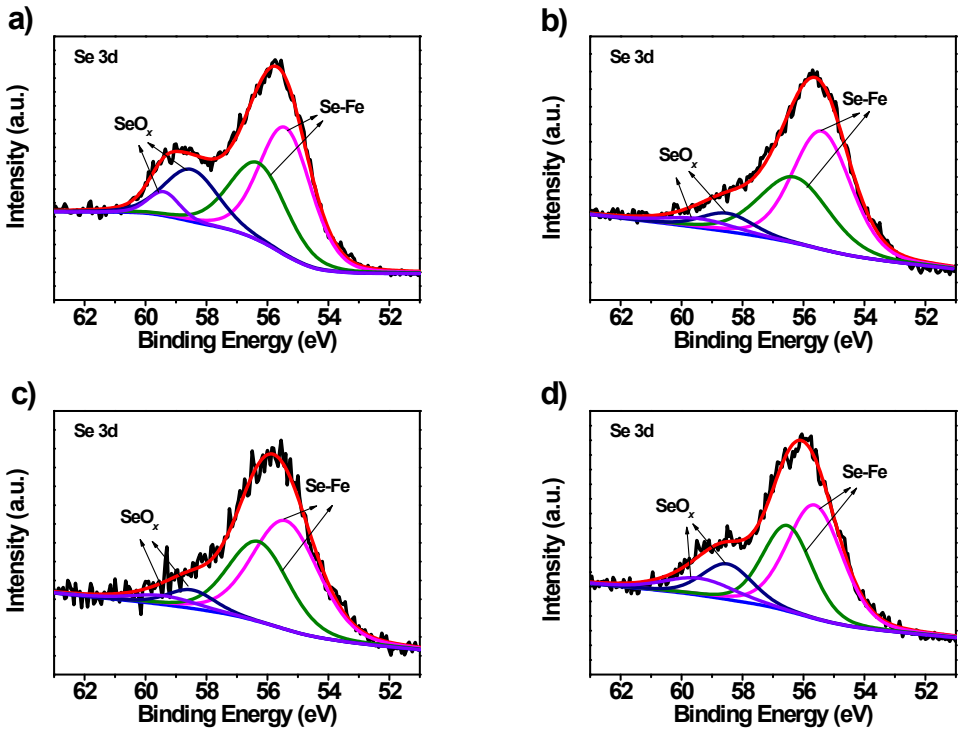

Fig. S15 High-resolution XPS spectra of Se 3d for a) FeSe@NC-700, b) FeSe@NC-800, c) FeSe@NC-900 and d) FeSe@NC-1000.

A set of peaks for Se-Fe bond were detected at 55.4/56.3 eV with a pair of weak peaks for SeO_x species at 58.5/59.4 eV. The Se-Fe bond is ascribed to FeSe.

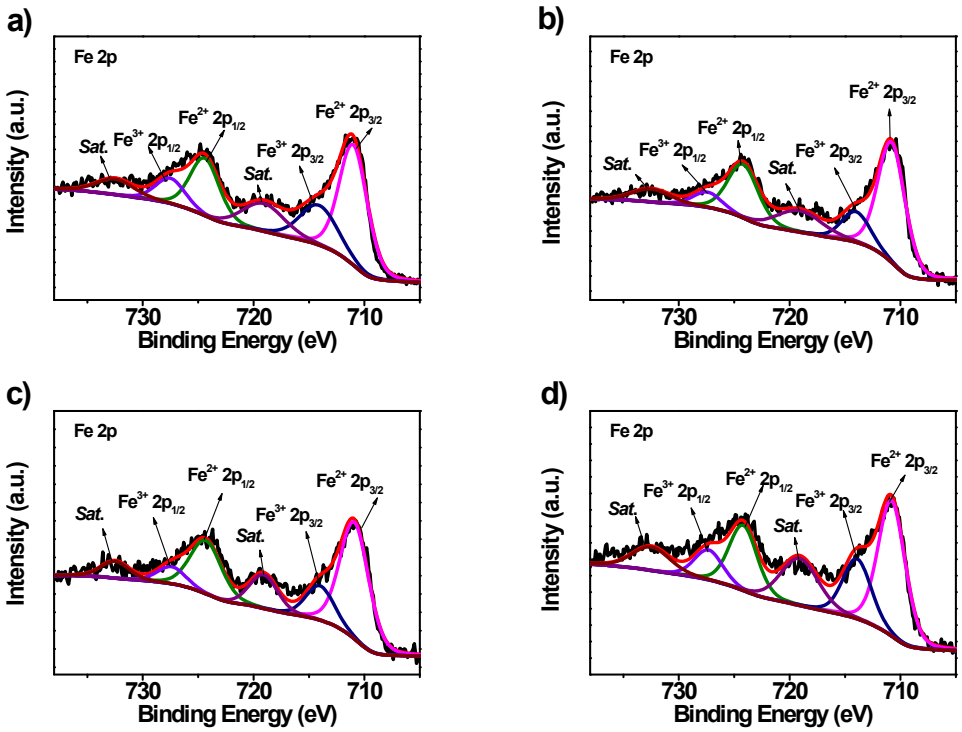

Fig. S16 High-resolution XPS spectra of Fe 2p for a) FeSe@NC-700, b) FeSe@NC-800, c) FeSe@NC-900 and d) FeSe@NC-1000.

The Fe 2p spectra were fitted by three pairs of spin-orbit doublets, which were related to ferrous (Fe^{2+}), ferric (Fe^{3+}) and shake-up satellites (abbreviated as "*Sat.*") with their binding energies located at 711.0/724.0 eV, 714.4/727.4 eV and 719.1/732.5 eV, respectively.

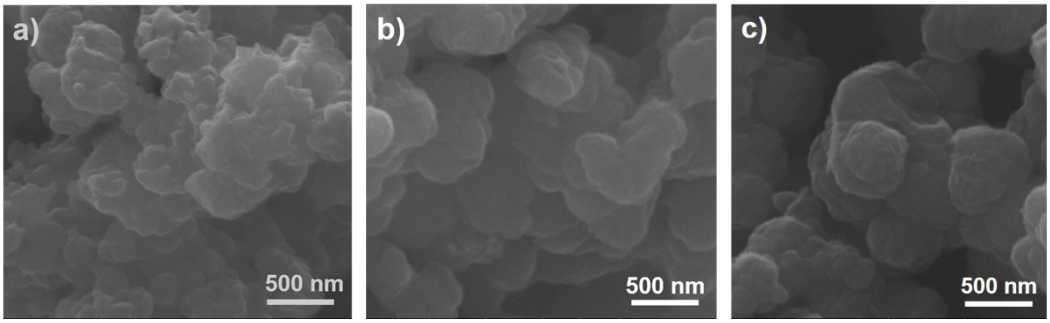

Fig. S17 SEM images of a) FeSe@NC-700, b) FeSe@NC-800 and c) FeSe@NC-900.

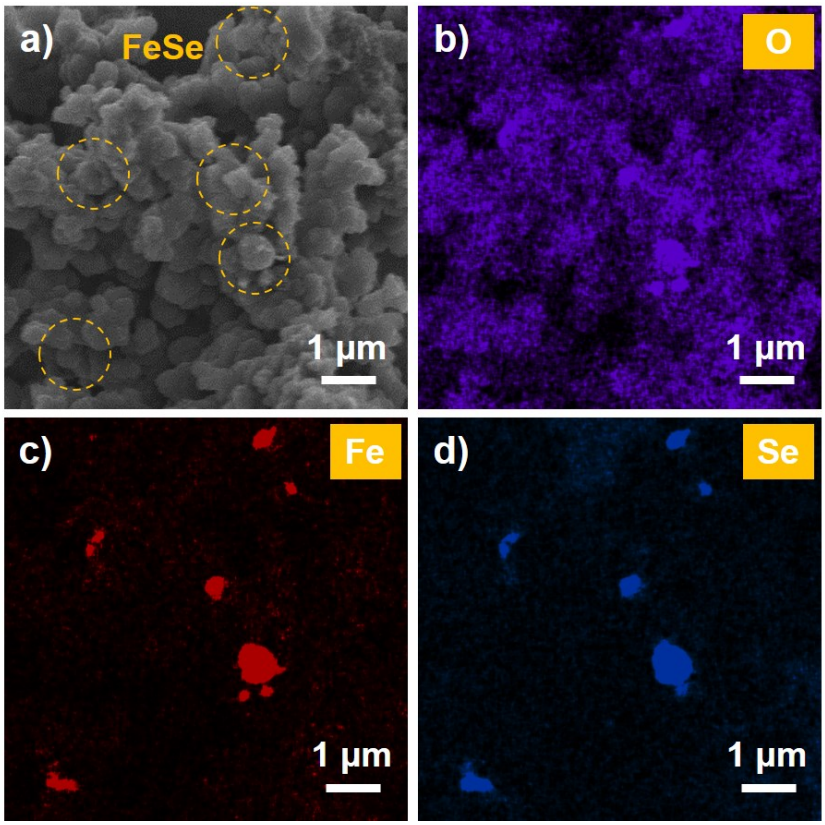

Fig. S18 a) SEM image and b-d) elemental mapping images of FeSe@NC-1000. Plenty of agglomerated FeSe particles were exposed on the surface of carbon skeletons.

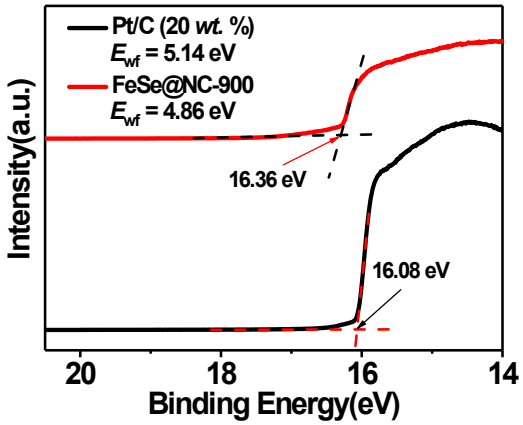

Fig. S19 Ultraviolet photoelectron spectra (UPS) for FeSe@NC-900 and commercial Pt/C (20 *wt.* %).

For UPS measurement, He I line (*hv* = 21.22 eV) was used as the gun source. The work function is equal to the difference between the energy of He I line and the cut-off energy of secondary electron.

Table S2. ICP results of the electrolyte (1.0 M KOH). There were no detectable transition metal elements.

Sample[a)]	Fe [mg L^{-1}]	Co [mg L^{-1}]	Ni [mg L^{-1}]
#1	---	---	---
#2	---	---	---

[a)] The testing solution was prepared by acidification with concertrated HNO_3 to fulfill ICP requirement. Solution #1 and #2 were parallel tests.

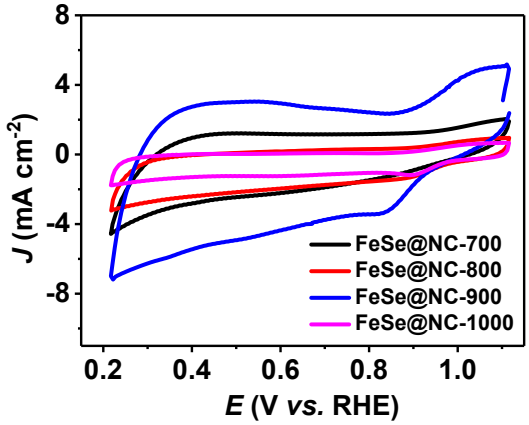

Fig. S20 CV curves of FeSe@NC-*T* materials acquired at a sweep rate of 100 mV s^{-1} in O_2-saturated 0.1 M KOH solution.

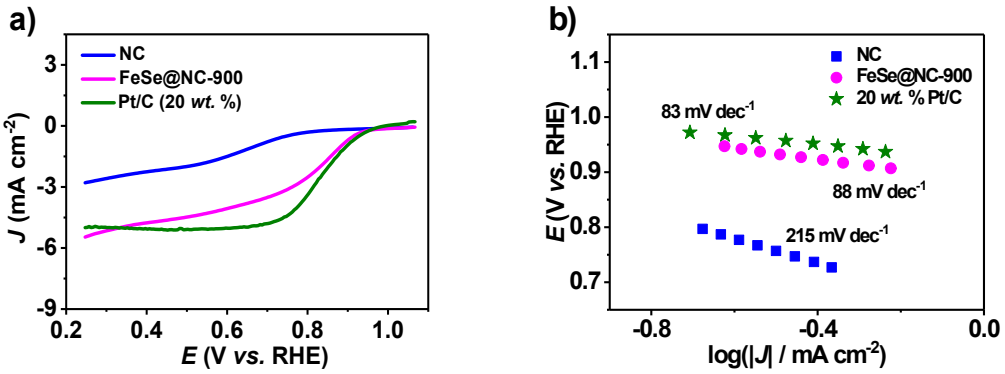

Fig. S21 a) LSV curves and b) Tafel plots of Pt/C, FeSe@NC-900 and NC. The Tafel plots were obtained by converting the LSV curves with Tafel formula. The Tafel slope was equal to the slope of Tafel plot.

Table S3. Comparison of the ORR performance of FeSe@NC-900 with respect to some recently reported electrocatalysts in alkaline solution.

Sample	*Conc.* of KOH [M]	E_0 [V][a)]	$E_{1/2}$ [V][b)]	J_L [mA cm^{-2}][c)]	Electron Transfer Number (*n*)	Reference
ZnCo-NC	0.1	0.94	0.82	-5.3	3.9	[1]
$SrMnO_3$	0.1	0.90	0.81	-4.6	3.9	[2]
N-CoS_2 YSSs	0.1	0.95	0.81	-5.6	3.7	[3]
Co_9S_8/G	0.1	0.87	0.72	-4.2	---	[4]
Co_9S_8@G/NSCNT	0.1	0.91	0.83	-5.5	3.7	[5]
$(Cu, Co)_3OS_3$@CNT-C_3N_4	0.1	0.91	0.80	-5.0	3.9	[6]
Ru/HNCS	0.1	0.83	0.72	-4.3	4.0	[7]
Co-S/SNGX	0.1	0.90	0.66	-4.6	3.9	[8]
Fe-N-C-800	0.1	0.89	0.72	-3.9	3.5	[9]
Ag-Mn Nanoplates	0.1	0.90	0.80	-5.8	3.9	[10]
p-Fe–N-CNF	0.1	0.91	0.82	-5.05	3.5	[11]
NC@Co-NGC DSNCs	0.1	0.92	0.82	-5.3	4.0	[12]
FeSe@NC-900	**0.1**	**0.97**	**0.80**	**-5.4**	**3.9**	**This work**

[a)] E_0 represents the onset potential; [b)] $E_{1/2}$ represents the half potential; [c)] J_L represents the limited current density.

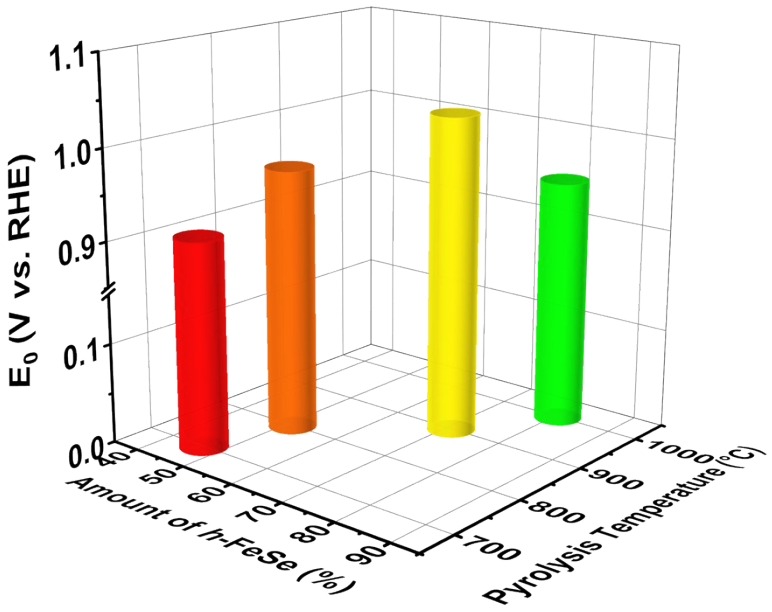

Fig. S22 Relationships between onset potential (E_0) and amount of *h*-FeSe in FeSe@NC-*T* (*T* = 700, 800, 900 and 1000 °C) materials for ORR. FeSe@NC-900 exhibits the most positive onset potential (E_0) among all materials.

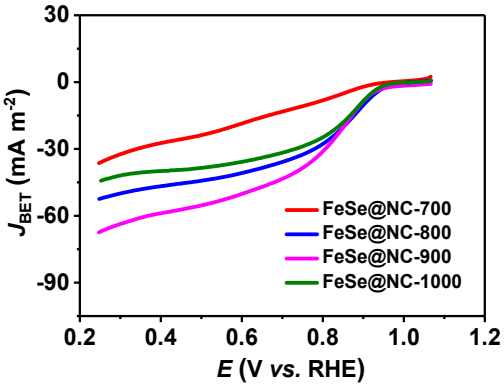

Fig. S23 The ORR activities normalized by corresponding BET surface areas of FeSe@NC-*T* (*T* = 700, 800, 900 and 1000 °C) materials.

Here, the value of J_{BET} is calculated by the following equation:

$$J_{BET} = \frac{J}{m \times S_{BET}}$$

where *J* is the current density normalized by electrode's surface area, *m* is the loading of electrocatalyst on the electrode, S_{BET} is the BET surface area.

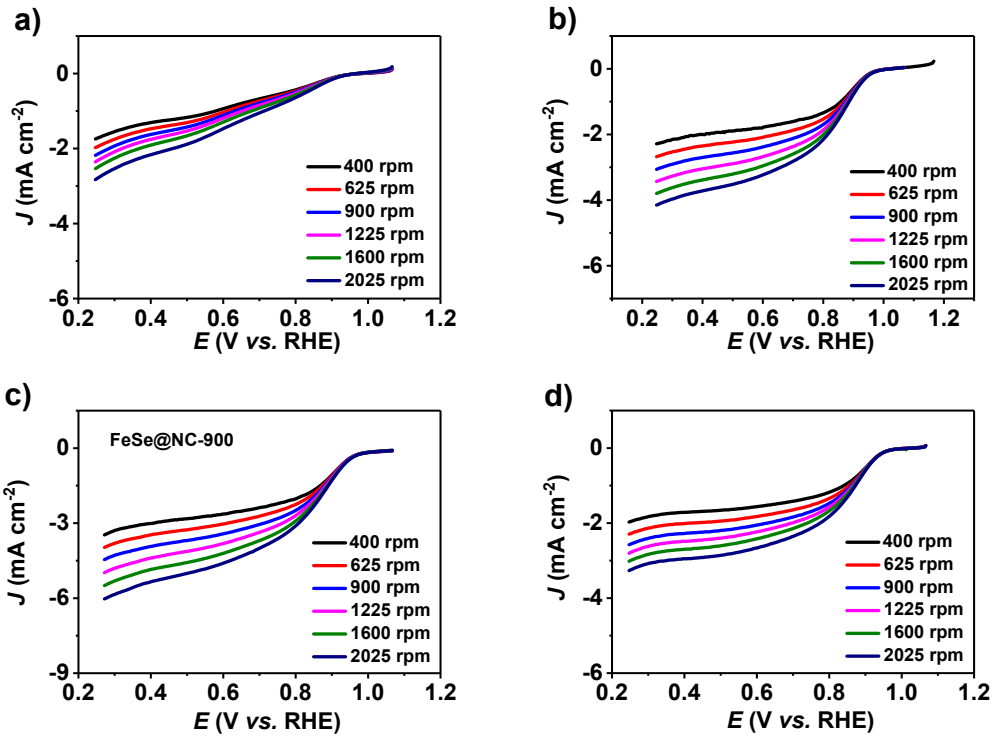

Fig. S24 Polarization curves of ORR for a) FeSe@NC-700, b) FeSe@NC-800, c) FeSe@NC-900 and d) FeSe@NC-1000 in O_2-saturated 0.1 M KOH solution.

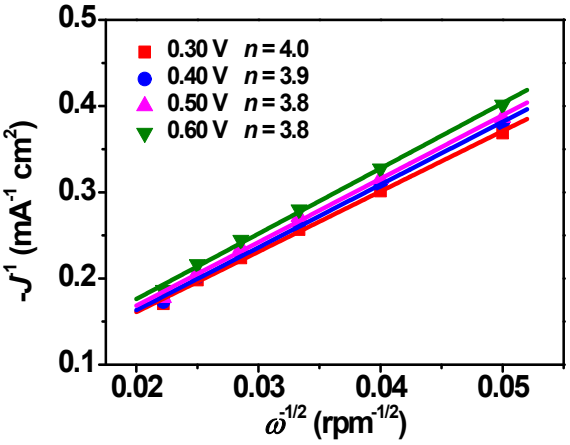

Fig. S25 Koutecky-Levich (K-L) plots of FeSe@NC-900 at different potentials. The excellent linearity indicates a first-order reaction kinetics with respect to the dissolved oxygen concentration.

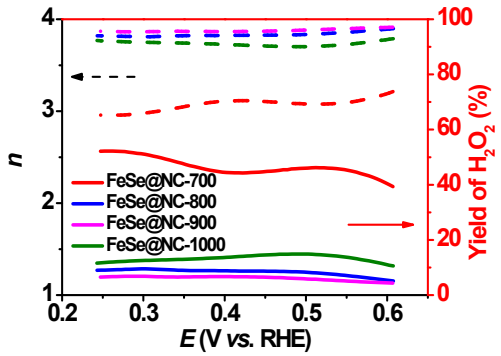

Fig. S26 Peroxide yield (solid line) and electron transfer number (dashed line) of FeSe@NC-*T* materials during ORR determined by the rotating ring-disk electrode (RRDE) technique.

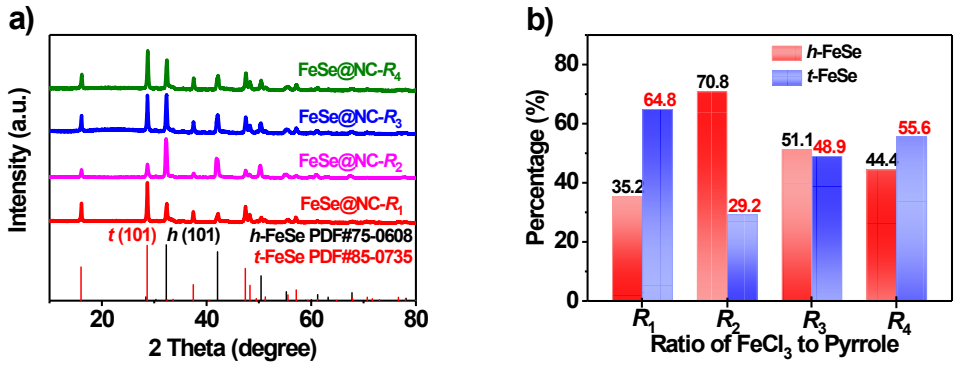

Fig. S27 a) XRD patterns and b) quantitative results obtained by Rietveld refinement for FeSe@NC-*R* materials (R_1 = 1/1, R_2 = 2.4/1, R_3 = 3/1, and R_4 = 4/1). FeSe@NC-R_2 is identical to FeSe@NC-900. All FeSe@NC-*R* materials were synthesized at the pyrolysis temperature of 900 °C.

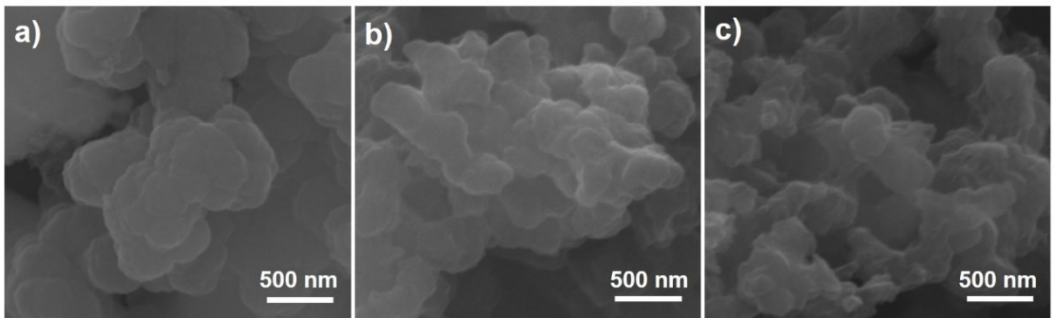

Fig. S28 SEM images of a) FeSe@NC-R_1, b) FeSe@NC-R_3 and c) FeSe@NC-R_4.

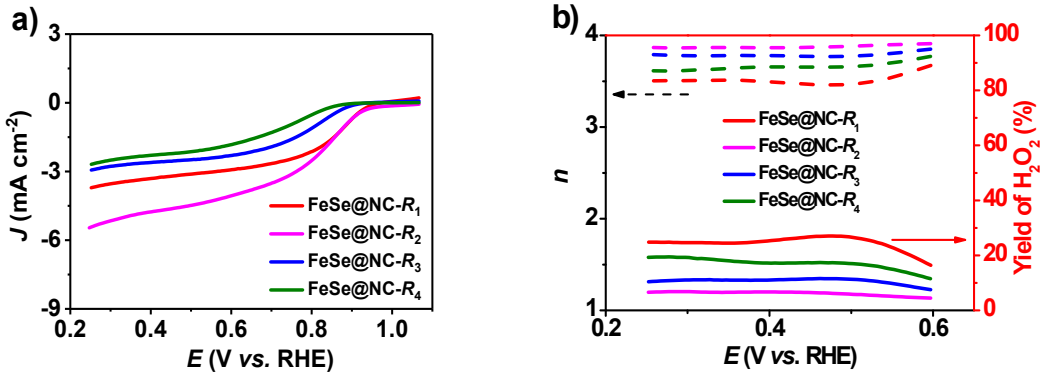

Fig. S29 a) LSV curves and b) Peroxide yield (solid line) and electron transfer number (dashed line) of FeSe@NC-*R* materials towards ORR at a rotating speed of 1600 rpm in O_2-saturated 0.1 M KOH solution. FeSe@NC-R_2 is identical to FeSe@NC-900.

Table S4. Electrochemical and electrocatalytic properties towards ORR over FeSe@NCs and NC in O_2-saturated 0.1 M KOH solution.

Sample	E_0 [V]	$E_{1/2}$ [V]	J_L [mA cm^{-2}]	Electron Transfer Number (n)[a)]	Selectivity of peroxide [%][b)]
FeSe@NC-700	0.91	0.61	-2.5	3.7	14.1
FeSe@NC-800	0.97	0.81	-3.8	3.8	8.7
FeSe@NC-900 (FeSe@NC-R_2)	1.03	0.78	-5.4	3.9	6.6
FeSe@NC-1000	0.95	0.82	-3.0	3.1	44.3
FeSe@NC-R_1	0.95	0.82	-3.7	3.5	26.0
FeSe@NC-R_3	0.90	0.76	-2.9	3.8	11.2
FeSe@NC-R_4	0.87	0.69	-2.7	3.7	17.2

[a, b)] Obtained from the graphs of peroxide selectivity and electron transfer number (n) versus potential at 0.20 V (*vs.* RHE).

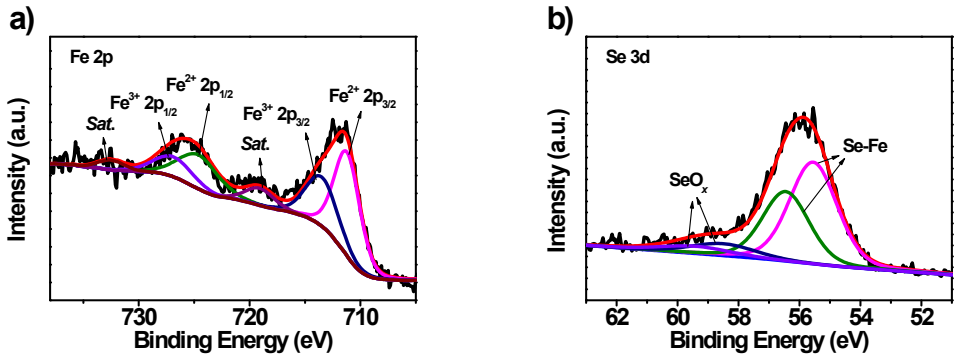

Fig. S30 High-resolution XPS spectra of a) Fe 2p and b) Se 3d for the FeSe@NC-900 material after stability test of 13 h.

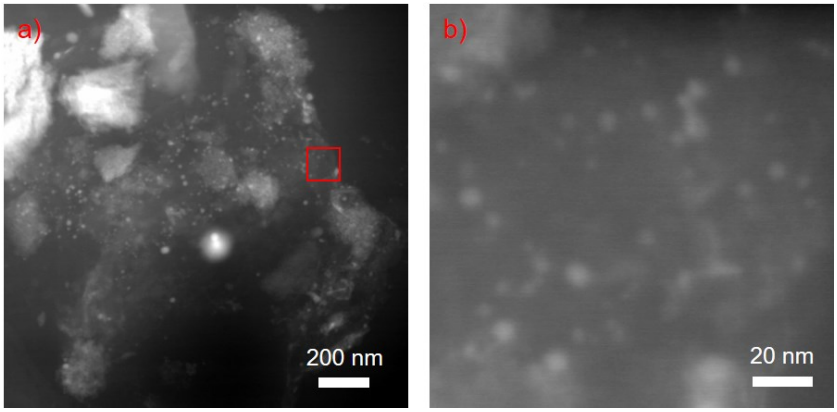

Fig. S31 HAADF images of FeSe@NC-900 after stability test of 13 h. Fig. b was acquired from the red marked region of Fig. a at high resolutions.

In the HAADF images of FeSe@NC-900 material after stability test of 13 h, there were still lots of bright dots dispersed in the carbon matrix, which were corresponded to ultrafine FeSe nanocrystals. Therefore, the material kept excellent structural stability for long-term ORR catalysis.

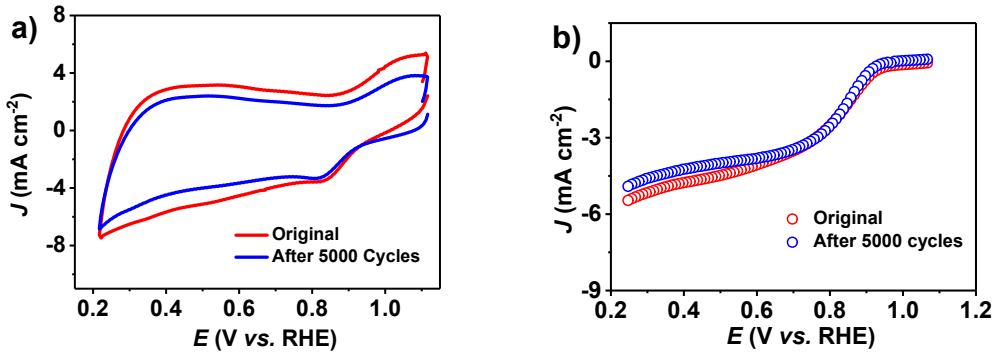

Fig. S32 Electrocatalytic ORR performances before and after the ADT test. a) CV scans and b) polarization curves.

The accelerated durability test (ADT) was referred to the typical literature (*J. Am. Chem. Soc.* 2015, 137, 15478). It was conducted under O_2-saturated condition for continuous 5000 cycles between 0.6 - 1.0 V vs. RHE. There is only little change in the current density after 5000 cycles of ADT test in both CV and polarization curves. The results are consistent with the chronoamperometry test, further confirming the excellent long-term catalytic stability of the material.

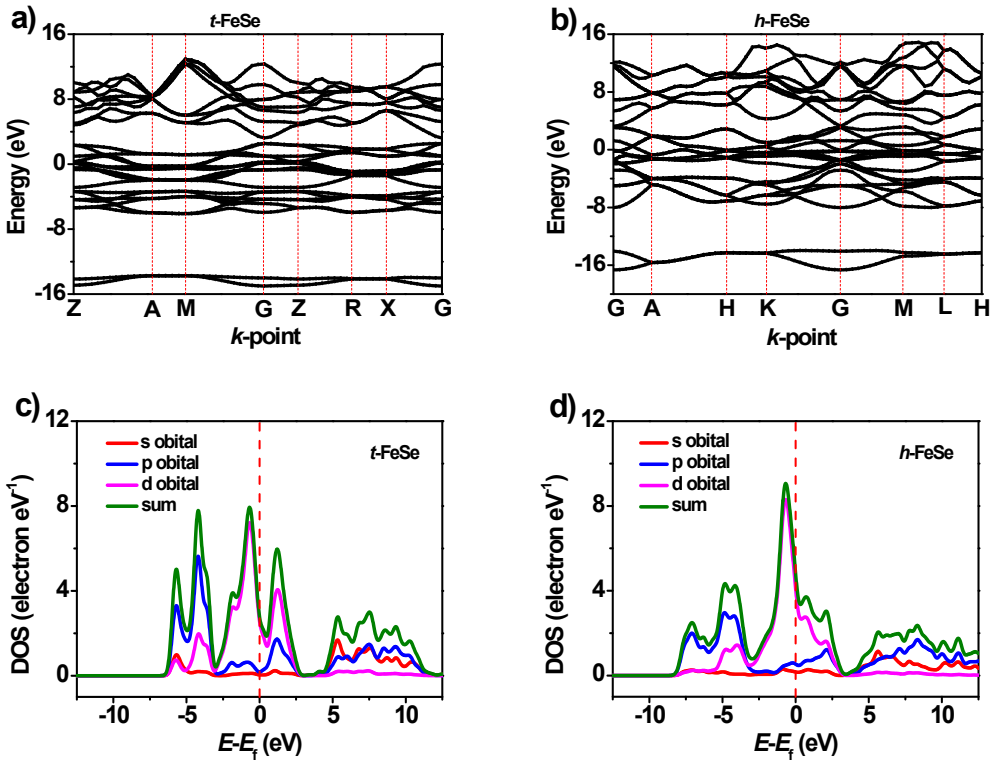

Fig. S33 a,b) Band structure and c,d) Density of states (DOS) of *t*-FeSe and *h*-FeSe. E_f is the energy of Fermi level. Both *t*-FeSe and *h*-FeSe were metallic with high electron population across the Fermi level.

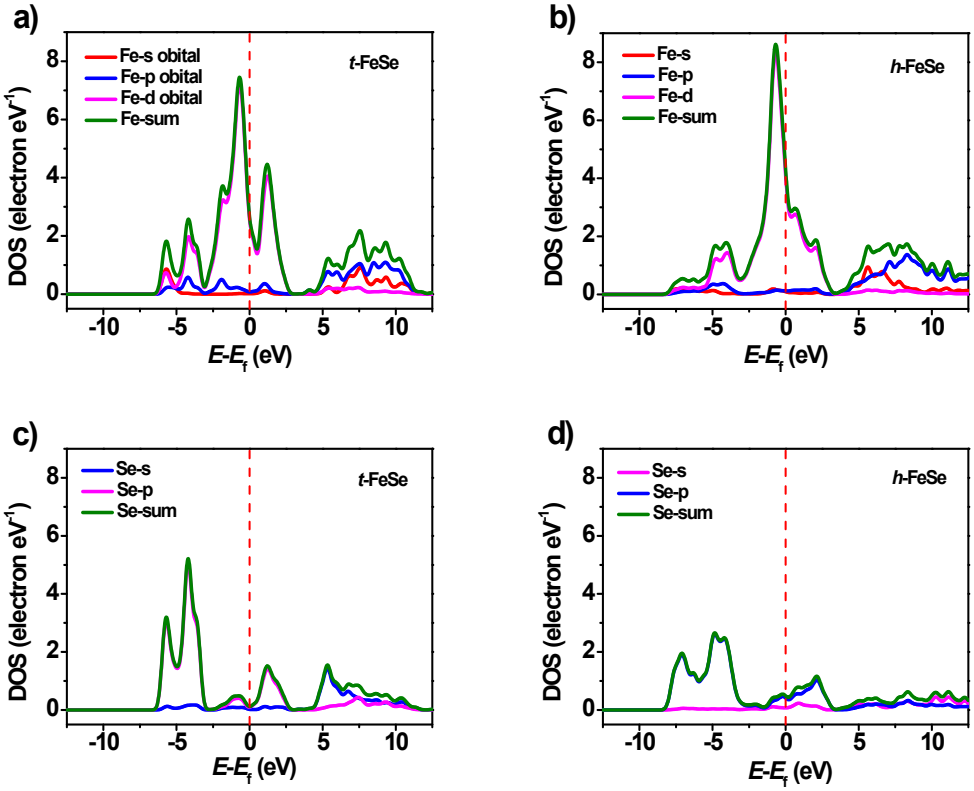

Fig. S34 Partial density of states (PDOS) of *t*-FeSe and *h*-FeSe from the view of a,b) Fe atoms and c,d) Se atoms.

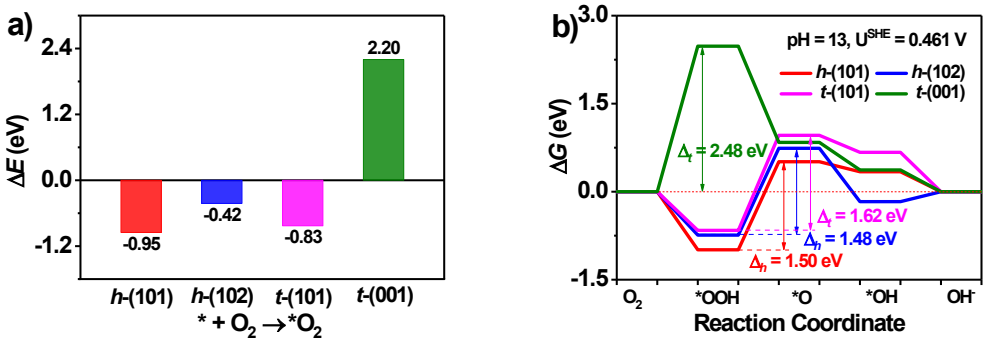

Fig. S35 a) O_2 adsorption energies and b) Gibbs free energies diagram of every ORR step on different crystal planes of *t*-FeSe and *h*-FeSe.

According to the XRD patterns, the dominated crystal planes of *h*-FeSe were (101) and (102) planes with strong peaks at 32.4 ° and 41.9 °, while those of *t*-FeSe were (001) and (101) planes with obvious peaks at 16.1 ° and 28.7 °, respectively. For simplicity, we focused our first-principles DFT calculations on these four planes while

neglecting the catalytic contributions from other planes due to their low diffraction intensity in the XRD patterns. Our theoretical calculations showed that, for *h*-FeSe, O_2 adsorption on (101) and (102) planes were both exothermic, and the potential determining step of whole reaction was very close (1.50 eV for (101) plane and 1.48 eV for (102) plane). In other words, the (101) plane of *h*-FeSe was almost as active as the (102) plane in nature towards ORR. Since the diffraction intensity of (101) plane was much stronger than that of (102) plane in the XRD patterns, the (101) plane would make the greatest catalytic contribution in ORR for *h*-FeSe. In the case of *t*-FeSe, (001) plane showed very high endothermicity for O_2 adsorption and large energy barrier for O_2 protonation into OOH intermediate, and is thus not catalytically active. The (101) plane of *t*-FeSe was the most active plane in ORR due to favorable O_2 adsorption and moderate energy barrier (1.62 eV) in the potential determining step of reaction. Overall, (101) planes of both *t*-FeSe and *h*-FeSe were regarded as the motive active planes to compare their ORR activities.

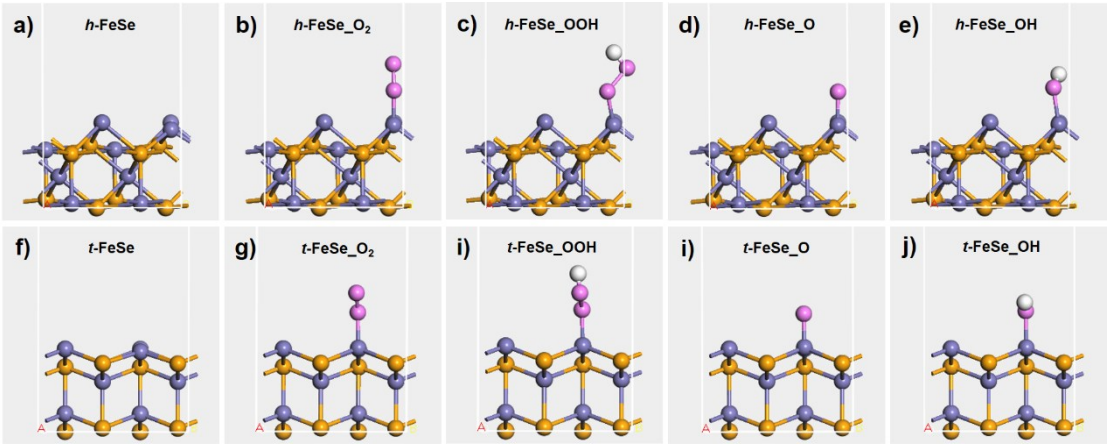

Fig. S36 Optimized models of initial FeSe models and those adsorbed with reactant or intermediates (*e.g.*, *O_2, *OOH, *O, *OH). The reactant is absorbed on the (101) plane of FeSe.

Table S5. The Fe-O and O-O bond lengths, as well as DFT energies of different models.

Model	Hexagonal FeSe (*h*-FeSe)		Tetragonal FeSe (*t*-FeSe)	
	Fe-O [Å]	O-O [Å]	Fe-O [Å]	O-O [Å]
O_2	---	1.239	---	1.239
FeSe	---	---	---	---
FeSe_O_2	1.680	1.286	1.717	1.294
FeSe_OOH	1.734	1.555	1.706	1.543
FeSe_O	1.630	---	1.618	---
FeSe_OH	1.803	---	1.776	---

References

[1] B. Chen, X. He, F. Yin, H. Wang, D. Liu, R. Shi, J. Chen and H. Yin, *Adv. Funct. Mater.*, 2017, **27**, 1700795-1700808.

[2] C. Zhao, X. Zhang, M. Yu, A. Wang, L. Wang, L. Xue, J. Liu, Z. Yang and W. Wang, *Adv. Mater.*, 2020. DOI: 10.1002/adma.202006145

[3] X. Lu, S. L. Zhang, E. Shangguan, P. Zhang, S. Gao and X. W. Lou, *Adv. Sci.*, 2020, **7**, 2001178.

[4] S. Dou, L. Tao, J. Huo, S. Wang and L. Dai, *Energy Environ. Sci.*, 2016, **9**, 1320-1326.

[5] N. Jia, J. Liu, Y. Gao, P. Chen, X. Chen, Z. An, X. Li and Y. Chen, *ChemSusChem*, 2019, **12**, 3390-3400.

[6] X. Wang, L. Peng, N. Xu, M. Wu, Y. Wang, J. Guo, S. Sun and J. Qiao, *ACS Appl. Mater. Interfaces*, 2020. DOI: 10.1021/acsami.0c16760

[7] A. Jiang, Z. Wang, Q. Li and M. Dong, *Mater. Today Phys.*, 2021, **16**, 100300.

[8] G. He, M. Qiao, W. Li, Y. Lu, T. Zhao, R. Zou, B. Li, J. A. Darr, J. Hu, M. M. Titirici and I. P. Parkin, *Adv. Sci.*, 2017, **4**, 1600214-1600223.

[9] M. Sun, D. Davenport, H. Liu, J. Qu, M. Elimelech and J. Li, *J. Mater. Chem. A*, 2018, **6**, 2527-2539.

[10] J. Ryu, H. Jang, J. Park, Y. Yoo, M. Park and J. Cho, *Nat. Commun.*, 2018, **9**, 3715.

[11] B. Hu, Z. Wu, S. Chu, H. Zhu, H. Liang, J. Zhang and S. Yu, *Energy Environ. Sci.*, 2018, **11**, 2208-2215.

[12] S. Liu, Z. Wang, S. Zhou, F. Yu, M. Yu, C. Y. Chiang, W. Zhou, J. Zhao and J. Qiu, *Adv. Mater.*, 2017, **29**, 1700874-1700883.